01 Apr 2022

Effect of Carbon Nanotube and Graphite Nanoplatelet on Composition, Structure, and Nano-Mechanical Properties of C-S-H in UHPC

Huanghuang Huang

Le Teng

Xiaojian Gao

Kamal Khayat
Missouri University of Science and Technology, khayatk@mst.edu

et. al. For a complete list of authors, see https://scholarsmine.mst.edu/civarc_enveng_facwork/2336

Recommended Citation

H. Huang et al., "Effect of Carbon Nanotube and Graphite Nanoplatelet on Composition, Structure, and Nano-Mechanical Properties of C-S-H in UHPC," *Cement and Concrete Research*, vol. 154, article no. 106713, Elsevier, Apr 2022.
The definitive version is available at https://doi.org/10.1016/j.cemconres.2022.106713

Cement and Concrete Research 154 (2022) 106713

Contents lists available at ScienceDirect

Cement and Concrete Research

journal homepage: www.elsevier.com/locate/cemconres

Effect of carbon nanotube and graphite nanoplatelet on composition, structure, and nano-mechanical properties of C-S-H in UHPC

Huanghuang Huang [a,b,c], Le Teng [d], Xiaojian Gao [b,*], Kamal H. Khayat [d,*], Fazhou Wang [a,c], Zhichao Liu [a,c]

[a] School of Materials Science and Engineering, Wuhan University of Technology, Wuhan 430070, China
[b] School of Civil Engineering, Harbin Institute of Technology, Harbin 150090, China
[c] State Key Laboratory of Silicate Materials for Architectures, Wuhan University of Technology, Wuhan 430070, China
[d] Department of Civil, Architectural and Environmental Engineering, Missouri University of Science and Technology, Rolla, MO 65401, USA

ARTICLE INFO

Keywords:
Carbon nanotube
C-S-H
Graphite nanoplatelet
Nano-mechanical properties
UHPC

ABSTRACT

This paper studied the influence of carbon nanotube (CNT) and graphite nanoplatelet (GNP) used at 0 to 0.3%, by mass of binder, on composition, structure, and nano-mechanical characteristics of C-S-H of ultra-high performance concrete (UHPC). Hydration kinetics, pore structure, and mechanical properties of UHPC were also investigated. The non-proprietary UHPC was proportioned with 17% lightweight sand for internal curing. Test results indicated that the addition of 0.3% CNT or GNP led to approximately 20 MPa increase in compressive strengths of non-fibrous UHPC mortar and fibrous UHPC (2% steel fibers), compared to those prepared without any nanomaterial. Such enhancement is attributed to the nucleation and filling effect of the nanomaterials that can refine the pore structure. The increase in CNT and GNP contents from 0 to 0.3% increased the proportion of high density and ultra-high density C-S-H from 65% to 90%. This led to a 20% greater elastic modulus of the C-S-H. The use of CNT and GNP also favored the transformation from Q^0 and Q^1 to Q^2 and Q^3 (Q^n represents the connectivity of silicate tetrahedron, and larger n indicates greater connectivity). This led to 140% and 110% increase in the mean chain length of C-S-H with the use of 0.3% CNT and GNP, respectively. Moreover, the Ca/Si of C-S-H decreased from 2.25 to 1.75, and the Al/Si increased from 0.1 to 0.15. The increased degree of Al—Si substitution reflects an enhanced pozzolanic reaction of the fly ash with the use of CNT and GNP.

1. Introduction

In recent years, the use of carbon nanomaterials, such as carbon nanotube (CNT) and graphite nanoplatelet (GNP) in cement-based materials has been attracting increasing interests given their outstanding mechanical and electrical properties [1–3]. The elastic moduli of CNT and GNP are on the order of 300 to 1000 GPa [4,5]. Molecular mechanical simulations indicated that the fracture strains of the nanomaterials ranged from 10% to 15%, with corresponding tensile strength on the order of 65 to 125 GPa [4,6].

Ultra-high performance concrete (UHPC) can exhibit very high mechanical properties and superior durability [7–9]. UHPC is proportioned with high content of binder materials, fine sand, steel fibers, and high-range water-reducer (HRWR) at a very low *w/b* based on optimal packing of the raw materials [10–12]. Steel fibers are used to improve compressive and tensile (flexural) strengths as well as toughness given their crack-bridging capacity [13,14].

Although the use of zero-dimensional (0-D) shape nanoparticles, such as nano-SiO_2 and nano-$CaCO_3$, is shown to increase the mechanical properties of UHPC, relatively high content of these materials is needed to enhance performance [15–17]. For example, the optimal contents to improve compressive and flexural strengths of UHPC were 1.5% for nano-SiO_2 and 4.8% for nano-$CaCO_3$, which led to 15% and 20% increase in compressive and flexural strengths, respectively [15]. Higher additions of nano-SiO_2 and nano-$CaCO_3$ of 2% and 6.4%, respectively, resulted in reduction in mechanical properties due to difficulties in ensuring proper dispersion [15].

On the other hand, CNT and GNP are 1-D and 2-D nanomaterials, respectively. CNT and GNP can be regarded as nanofibers given their length/diameter or diameter/thickness ratio on the order of 1000 [18,19]. Therefore, the use of CNT and GNP can enhance the nucleation effect [5,20], as well crack-bridging capability on the nanoscale level

* Corresponding authors.
E-mail addresses: gaoxj@hit.edu.cn (X. Gao), khayatk@mst.edu (K.H. Khayat).

https://doi.org/10.1016/j.cemconres.2022.106713
Received 23 August 2021; Received in revised form 2 November 2021; Accepted 8 January 2022
Available online 26 January 2022

[21–23]. This can lead to substantial improvement in mechanical properties of UHPC at low addition rates of 0.05% to 0.5% of CNT and GNP, by mass of binder [10,18,24,25]. For example, the addition of 0.067% CNT led to 70% increase in flexural strength of UHPC compared to that prepared without any CNT [25]. The use of 0.3% GNP enhanced the tensile strength and toughness of UHPC by 60% and 155%, respectively, compared to those made without GNP [10]. It can be concluded that the needed content is lower, and the improvement ratio in UHPC performance is greater for CNT and GNP compared to nano-SiO_2 and nano-$CaCO_3$. Such low additions of CNT and GNP can also benefit their dispersion.

Despite the significant improvement on mechanical properties discussed above, the influence of CNT and GNP on microstructure of UHPC, especially on the composition and structure of C-S-H under a low *w/b* is not fully understood. Changes in Ca/Si, Al/Si, and chain length were used to evaluate the evolution of composition and structure of C-S-H [26,27]. CNT and GNP, due to their nucleation effect, can affect the cement hydration, thus changing the Ca/Si and C-S-H chain length. For UHPC prepared with supplementary cementitious materials (SCMs) that have high content of Al, e.g., Class C fly ash, Al can substitute for Si given the pozzolanic reaction between SCMs and $Ca(OH)_2$, leading to the changes in Ca/Si and Al/Si [27,28]. However, the influence of CNT and GNP on the extent of Al—Si substitution is still not investigated.

In addition, the nano-mechanical characteristics of C-S-H can greatly influence compressive, flexural, and tensile properties of UHPC. Considering their elastic moduli, C-S-H phases are characterized as low density (LD), high density (HD), and ultra-high density (UHD) C-S-H, while the last only appears in UHPC [29–31]. The LD, HD, and UHD C-S-H correspond to elastic modulus values on the order of 10–25, 25–40, and 40–60 GPa, respectively, and a higher C-S-H elastic modulus indicates a greater contribution to mechanical properties of UHPC [29,30,32]. However, the influence of CNT and GNP on the elastic modulus of C-S-H and the proportion of each type of C-S-H is still not studied.

The knowledge gap discussed above can constrain the wider use of CNT and GNP in UHPC. Greater understanding of underlying mechanisms of these nanomaterials is needed to develop more advanced construction materials. The objective of this study is to elucidate the influence of CNT and GNP on the composition, structure and nano-mechanical characteristics of C-S-H in UHPC mortar. This includes the changes in Ca/Si, Al/Si, chain length, and elastic modulus of C-S-H with the use of CNT and GNP. The influence of CNT and GNP on cement hydration, mechanical properties, and pore structure of UHPC is also investigated. The content of CNT and GNP was increased from 0 to 0.3%, by binder mass. The results of the study can advance the acceptance and application of CNT and GNP as an important component of UHPC with improved mechanical and microstructural properties.

2. Experimental program

2.1. Raw materials and mixture design

Type III Portland cement, Class C fly ash (FAC), and silica fume (SF) were used as binder materials at ratios of 55%, 40%, and 5%, respectively, by binder volume. The chemical and physical properties of binder materials are listed in Table 1. River sand (RS, 0–4.75 mm), masonry sand (MS, 0-2 mm), and pre-saturated lightweight sand (LWS, 0–4.75 mm) were used at ratios of 53%, 30%, and 17%, respectively, by sand volume. The water absorption of LWS was 17.6%. The LWS was saturated by mixing with water and sealed in a plastic bucket for 48 h before use. Steel fibers with 13 mm in length and 0.2 mm in diameter were used at 2%, by mixture volume.

The CNT and GNP were investigated at contents of 0, 0.05%, 0.1%, 0.15%, 0.2%, and 0.3%, by mass of binder. Higher nanomaterial content was not investigated due to the difficulty in ensuring uniform dispersion of the nanomaterial. Nanomaterial content higher than 0.3% was found to have a limited effect on enhancing mechanical properties due to the agglomeration of the nanomaterial in matrix [33,34]. The material properties of used CNT and GNP are given in Tables 2 and 3, respectively.

Table 1
Chemical and physical properties of cement, SF, and FAC.

	Cement	SF	FAC
CaO (%)	64.50	0.40	28.10
SiO_2 (%)	19.72	95.50	36.50
Al_2O_3 (%)	5.10	0.70	24.80
Fe_2O_3 (%)	2.76	0.30	5.20
MgO (%)	2.30	0.50	5.00
Na_2O eq. (%)	0.33	0.40	–
SO_3	3.25	–	2.50
Loss of ignition (%)	1.50	2.00	0.50
Apparent density (g/m^3)	3.15	2.20	2.70
Blaine specific surface area (SSA) (m^2/kg)	562	–	465
B.E.T. SSA (m^2/g)	–	18.2	–

Polycarboxylate-based HRWR having a solid content of 26% was employed to secure a high fluidity. Welan gum powder (WG) was employed to adjust the mixture viscosity to secure a self-consolidating consistency. Air-detraining admixture (ADA) having a solid content of 5% was applied to reduce the entrapped air of mixture. HRWR and Polyacrylic acid (PAA) with 35% wt% in water was used as surfactants to favor the dispersion of CNT and GNP [35]. The average molecular weight of PAA is on the order of 250,000. The mixture proportion of UHPC mortar containing different nanomaterial contents is listed in Table 4. The mixture proportion of the UHPC corresponds to a non-proprietary mixture with target compressive strength of 120 MPa under wet curing condition at 20 °C, which meets the ASTM C1856 Standard. This mixture is considered as cost-effective UHPC with high volume of supplementary cementitious materials and conventional concrete and masonry sands [36]. It is important to note that the compressive strength of this mixture can easily exceed 150 MPa under heat/steam curing conditions [36].

2.2. Mixing, casting, and curing

The uniform dispersion of nanomaterial in fresh UHPC mixtures is essential to secure the high performance of hardened sample. The CNT and GNP were dispersed using the same method proposed in [33]. The CNT (or GNP), HRWR, and PAA were added into 600 mL mixing water with a mass ratio of 1:4:0.1. The liquid suspension containing nanomaterial, HRWR, and PAA was mixed for 4 h at 60 rpm followed by a 70-min high-intensity sonification treatment. The sonification was paused for 30 s every 60 s to avoid suspension overheating and equipment overloading.

UHPC mixtures were prepared using a 19-L Hobart mixer at 0.20 *w/b*. The WG was dispersed in the remaining HRWR by a magnetic mixer at 750 rpm for 10 min. Solid materials, including binders and sands were premixed at 60 rpm for 2 min. Then, 90% of the liquids, including the mixing water, pre-dispersed nanomaterial suspension, WG suspension, and ADA were added and mixed at 120 rpm for 3 min. The remaining liquids were then added and mixed at 120 rpm for 3 min. For UHPC mortar, the mixing was kept at 120 rpm for an additional 4 min to achieve an adequate mixture homogeneity. For fibrous UHPC, steel fibers were added into mortar in 1 min. The mixture containing fibers were mixed at 120 rpm for additional 3 min to secure an adequate fiber dispersion. A total of 12 min was needed for each mixing.

For each UHPC mixture, 50-mm cube samples were prepared in one lift for compressive strength test. The samples were cured at room temperature with coverage of plastic wraps and wet burlaps (immediately after casting) for 1 d followed by lime-saturated water curing at 21 ± 2 °C until 28 d.

Table 2
Properties of the used CNT.

Fiber type	Length (μm)	Outer diameter (nm)	Inner diameter (nm)	SSA (m^2/g)	Density (g/m^3)	Purity (wt%)	Elastic modulus (GPa)
CNT	<10	30–80	5–15	>80	2.1	>95%	1000

Table 3
Properties of the used GNP.

Fiber type	Thickness (nm)	Diameter (μm)	Number of platelets	SSA (m^2/g)	Density (g/m^3)	Purity (wt%)	Elastic modulus (GPa)
GNP	4–20	5–10	<20	>60	2	>99.5%	1010

Table 4
Mixture proportion of UHPC mortar prepared with various nanomaterial contents.

Cement (kg/m^3)	FAC (kg/m^3)	SF (kg/m^3)	RS (kg/m^3)	MS (kg/m^3)	LWS (kg/m^3)	WG (% by mass of binder)	ADA (% by mass of binder)	Nanomaterial contents (% by mass of binder)
662	413	42	527	308	120	0.18	0.8	0 0.05 0.1 0.15 0.2 0.3

2.3. Testing methods

2.3.1. Fresh properties

A mini-slump cone with upper diameter, lower diameter, and height measuring 70, 100, and 60 mm, respectively, was used to measure the mini-slump flow of mixture, according to ASTM C230/C230M. The air content was measured according to ASTM C138. The rheological properties of mixture were tested by the ConTec 5 rheometer. The mixture was pre-sheared for 25 s under rotational speed of 0.5 rps. The rotational speed then decreased from 0.5 to 0.025 rps in 10 steps. The data points measured at the highest two rotational speeds were removed due to the lack of equilibrium at the end of mixing. The remaining eight data points were used to determine the flow curves which were consistently linear. The plastic viscosity and yield stress were calculated using Bingham model based on the obtained flow curves.

2.3.2. Hydration kinetics

The hydration kinetics of mixtures containing different nanomaterial contents was determined through the isothermal conduction calorimetry (Calmetrix I-CAL 8000). Immediately after ending the mixing, approximately 75 g mixture was sealed in a plastic vial for test. The test continued for 48 h at a temperature of 20 ± 0.1 °C.

2.3.3. Mechanical properties

The 28-d compressive strength of non-fibrous UHPC mortar and fibrous UHPC (2% steel fiber volume) was determined based on three 50-mm cubes. The loading rate was 1.8 kN/min according to ASTM C109.

2.3.4. Nano-mechanical characteristics

Nano-mechanical characteristics of UHPC mortar prepared with different nanomaterial contents were determined using the Anton Paar Nano-indentation tester with a diamond Berkovich tip. Samples measuring 10 × 10 × 10 mm were taken out from the center of cubes. The hydration of samples was terminated using isopropyl alcohol at 28 d. The sample was impregnated with epoxy resin, and the surface of sample was polished successively using the 400, 600, and 1200 grit polishing papers. The sample surface was then polished using diamond abrasives with sizes of 9, 3, 1, and 0.25 μm [37,38]. The duration for each grade polishing was 3 min.

Fig. 1 illustrates the 8 × 10 grid for nano-indentation test points. For each sample, two 8 × 10 grids (160 points in total) were tested. The spacing of two adjacent test points of each grid was 20 μm. For each point, the test load linearly increased at a 10 mN/min rate to a maximum load of 5 mN. The maximum load was remained for 4 s and then linearly decreased at a same rate (10 mN/min).

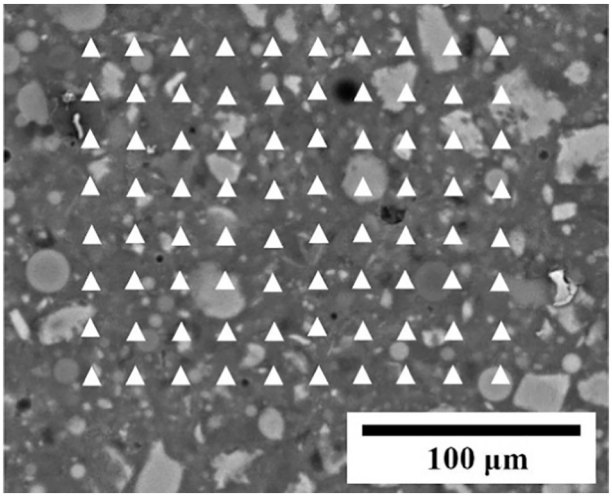

Fig. 1. Illustration of 8 × 10 grid for nano-indentation test points.

2.3.5. Backscattered electron (BSE) imaging

The sample after nano-indentation was used for the energy dispersion X-ray spectra (EDX) analysis using a Tescan VeGA 3 scanning electron microscope. The accelerating voltage and work distance of the test were 30 kV and 15 mm, respectively.

2.3.6. Mercury intrusion porosimetry

The pore structure of UHPC mortar prepared with different nanomaterial contents were evaluated using the IV 9510 MIP. Samples were kept in the isopropyl alcohol at 28 d to terminate hydration reactions and dried at 50 °C for 24 h before test. The low and high pressures of MIP test were 0.28 and 414 MPa, respectively.

2.3.7. Nuclear magnetic resonance spectroscopy (NMR)

The ^{29}Si and ^{27}Al NMR spectra of UHPC paste made with various nanomaterial contents were tested using the Bruker Solid-state NMR Spectrometer (400 MHz). The spin speeds for ^{29}Si and ^{27}Al NMR tests were 5 and 12 kHz, respectively. UHPC pastes made with different nanomaterial contents were ground into fine powder that has a particle size lower than 75 μm.

3. Results and discussion

3.1. Fresh properties

The fresh properties, given as mean values and coefficients of variation (COVs), of mixtures prepared with various nanomaterial contents are shown in Table 5. In this paper, the slump flow of UHPC mixtures prepared with different nanomaterial contents was fixed at 270 ± 10 mm by adjusting HRWR content. As demonstrated in the table, the HRWR demand decreased with the nanomaterial content increased to 0.1%. This can be due to the filling effect of nanomaterial that can result in an enhanced packing density of cementitious particles [33]. This can increase the fluidity of mixture, hence reducing the HRWR demand. However, further increase in nanomaterial content to 0.3% resulted in an increased HRWR demand. The high specific surface areas of CNT and GNP need additional mixing water to wet their surfaces [33,39]. When the nanomaterial content surpassed 0.1%, such effect became dominant compared to filling effect, resulting in a higher HRWR demand to secure a constant slump flow. Given a similar content, the HRWR demand of UHPC mixture made with CNT was slightly higher than that made with GNP. This can be due to the fact that CNT can absorb water molecules on its surface [40].

Given the constant slump flow of 270 ± 10 mm, the yield stress was shown to maintain at approximately 20 Pa with the changes in nanomaterial content. The plastic viscosity slightly decreased and then increased to approximately 34 Pa·s with the use of CNT and GNP. The decrease in plastic viscosity under a nanomaterial content of 0–0.1% is due to the increased packing density [41]. On the other hand, with the further increase of nanomaterial content, CNT or GNP can be absorbed on the surface of cement particles through the intermolecular force, which can reduce the steric hindrance and electrostatic repulsion of HRWR [42]. This can enhance flocculated structure in mixture, thus increasing the plastic viscosity.

The air content reduced when the nanomaterial content increased from 0 to 0.1%. Further increase in nanomaterial content to 0.3% increased the air content from 3.8% to 4.3%. This is due to the increased plastic viscosity that entrapped more air during mixing.

3.2. Compressive strength

The 28-d compressive strength of non-fibrous UHPC mortar and fibrous UHPC with 2% steel fibers containing various contents of CNT and GNP is shown in Fig. 2. For the non-fibrous UHPC mortar and fibrous UHPC made without any nanomaterial, the 28-d compressive strength was approximately 112 and 130 MPa, respectively. The compressive strength was significantly increased with the use of CNT and GNP. As the CNT and GNP contents increased to 0.3%, the 28-d compressive strength of non-fibrous UHPC mortar and fibrous UHPC was enhanced by approximately 20 MPa.

The improvement on mechanical properties was due to the nucleation and filling effect of CNT and GNP. The nucleation effect can promote cement hydration, and the filling effect can refine the pore structure of hardened sample, which are elaborated in Sections 3.3 and 3.4, respectively. Moreover, CNT and GNP can act as nanofibers that can delay the initiation of microcracks and bridge microcracks, leading to the enhancement in mechanical properties [10,21]. In addition, CNT has a higher specific surface area compared to that of GNP [21,43]. This can enable more nucleation sites for C-S-H. Therefore, samples prepared with CNT showed greater compressive and tensile strength compared to those prepared with GNP given a similar content.

3.3. Hydration kinetics

The hydration kinetics of UHPC mixtures containing different nanomaterial contents are presented in Fig. 3. The use of nanomaterial increased the peak heat flow and cumulative heat, compared to those of reference mixture. To analyze the variations in hydration process of UHPC mixtures containing different nanomaterial contents, several parameters are calculated from the hydration curves, as summarized in Table 6. t_A and t_B correspond to the ending time of the induction period and the time of peak heat flow, respectively. $(dQ/dt)_A$ and $(dQ/dt)_B$ represent the heat flow corresponding to t_A and t_B, respectively. Q_A and Q_B represent the cumulative heat corresponding to t_A and t_B, respectively. Q_{A-B} indicates the cumulative heat during the acceleration period.

As shown in the table, t_A and t_B were advanced when 0.1% nanomaterial was added compared to those of reference sample. This is in agreement with Section 3.1 where the HRWR demand decreased with the nanomaterial content increasing from 0 to 0.1%. On the other hand, further increase in nanomaterial content led to prolonged t_A and t_B. The t_A and t_B were prolonged by 0.2 h for mixtures prepared with 0.3% CNT. Such prolongation was 0.1 h for mixtures made with 0.3% GNP. This can be due to the increased HRWR molecules absorbed on the surface of cement particles, which retarded the dissolution of cement particles [44].

With the changes of CNT and GNP content, $(dQ/dt)_A$ and Q_A varied slightly. On the other hand, $(dQ/dt)_B$, Q_B, and Q_{A-B} were enhanced by approximately 15%, 46%, and 51%, respectively, by adding CNT from 0 to 0.3%. Such enhancements in $(dQ/dt)_B$, Q_B, and Q_{A-B} for GNP were 12%, 36%, and 42%, respectively. The hydration rate in the acceleration period mainly depends on the nucleation sites of C-S-H [45]. The enhancement of nanomaterial content significantly increased the

Table 5
Fresh properties of mixtures prepared with various nanomaterial contents.

Nanomaterial content	HRWR demand (%)[a]	COV (%)	Air content (%)	COV (%)	Yield stress (Pa)	COV (%)	Plastic viscosity (Pa·s)	COV (%)
Ref	0.42	2.8	3.8	4.6	20.7	3.5	29.7	2.8
CNT0.05%	0.4	4.1	3.75	5.2	20	2.4	28.9	3.6
CNT0.1%	0.41	3.5	3.8	5.8	21.5	3.2	28.8	3.1
CNT0.15%	0.42	5.2	3.95	4.2	21.3	3.8	29.8	4.2
CNT0.2%	0.435	3.7	4.15	3.3	22.5	2.9	31.4	3.6
CNT0.3%	0.45	4.3	4.3	5.1	23.2	4.0	33.6	3.3
GNP0.05%	0.4	2.6	3.7	4.8	19.6	2.5	27.6	2.6
GNP0.1%	0.405	3.4	3.8	6.4	20.3	3.4	28.6	3.6
GNP0.15%	0.415	5.3	4	4.7	22.4	3.3	29.4	4.1
GNP0.2%	0.425	4.6	4.1	4.5	21.9	2.7	30.9	3.8
GNP0.3%	0.445	3.4	4.2	5.4	22.7	3.8	32.8	3.4

[a] Active portion, by mass of binder.

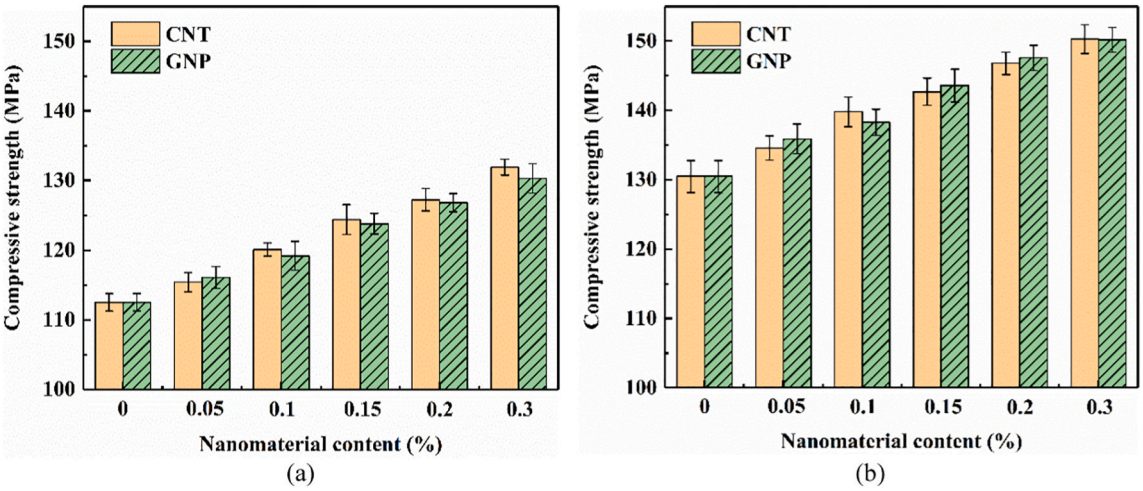

Fig. 2. 28-d compressive strength of (a) non-fibrous UHPC mortar and (b) fibrous UHPC (2% steel fibers) prepared with different nanomaterial contents.

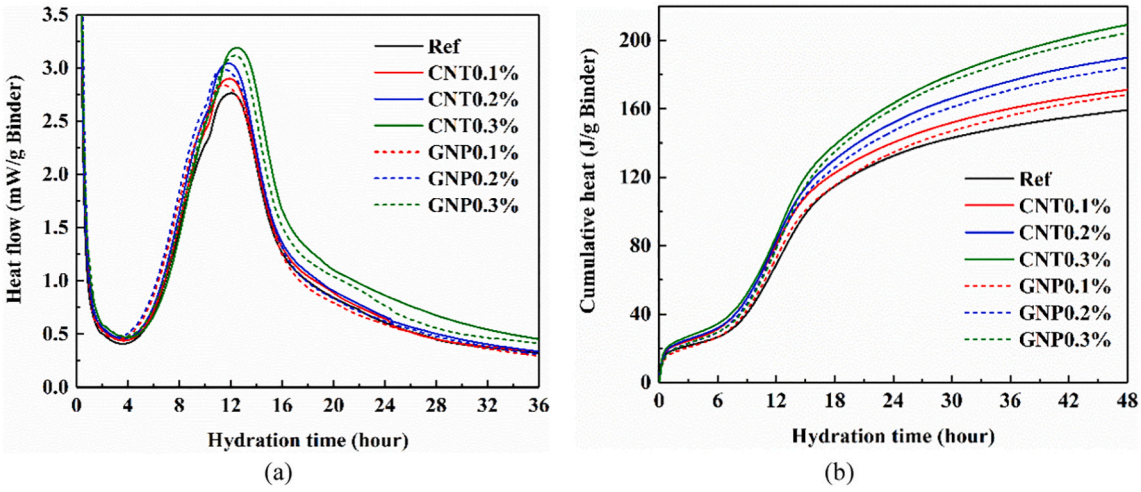

Fig. 3. (a) Heat flow and (b) cumulative heat of mixtures prepared with different nanomaterial contents.

Table 6
Parameters calculated from the hydration curves of mixtures prepared with various nanomaterial contents.

Nanomaterial content	t_A (h)	$(dQ/dt)_A$ (mW/g binder)	Q_A (J/g binder)	t_B (h)	$(dQ/dt)_B$ (mW/g binder)	Q_B (J/g binder)	Q_{A-B} (J/g binder)
Ref	3.65	0.41	21.15	12.03	2.76	62.53	41.38
CNT0.1%	3.6	0.44	26.11	11.9	2.9	77.57	51.46
CNT0.2%	3.71	0.46	27.17	12.06	3.04	84.05	56.88
CNT0.3%	3.83	0.47	28.64	12.25	3.18	91.25	62.61
GNP0.1%	3.5	0.43	20.52	11.78	2.82	68.91	48.39
GNP0.2%	3.55	0.45	24.91	11.93	2.96	77.25	52.34
GNP0.3%	3.75	0.48	26.6	12.15	3.11	85.16	58.56

number of nucleation sites, thus resulting in the increased values of $(dQ/dt)_B$, Q_B, and Q_{A-B}. In addition, the $(dQ/dt)_B$, Q_B, and Q_{A-B} values of mixtures prepared with CNT were slightly higher than those made with a similar GNP content, which is consistent with the mechanical strength results. This is possibly attributed to the greater specific surface area of CNT compared to that of GNP, which can provide more nucleation sites of C-S-H [21,43].

3.4. Pore structure

Fig. 4 shows the distribution of pore size for samples made with various nanomaterial contents. The pore size corresponding to the peak of the curve refers to the most probable diameter. With the increase of nanomaterial content, the most probable diameter shifted to finer pore size. Similar results were reported in [33] where the addition of CNF was found to refine the pore structure of UHPC mortar. Therefore, it can be concluded that the use of CNT and GNP can result in refinement in the pore structure of UHPC mortar. Such refined pore structure led to the improvement in mechanical properties.

Pores in concrete can be classified as gel pores, capillary pores, and macro-pores with diameter of <10, 10–5000, and >5000 nm, respectively [46]. Fig. 5 exhibits the total porosity and the porosity of each type of pore for samples prepared with different CNT and GNP contents. For UHPC samples made without nanomaterial, the 28-d total porosity is

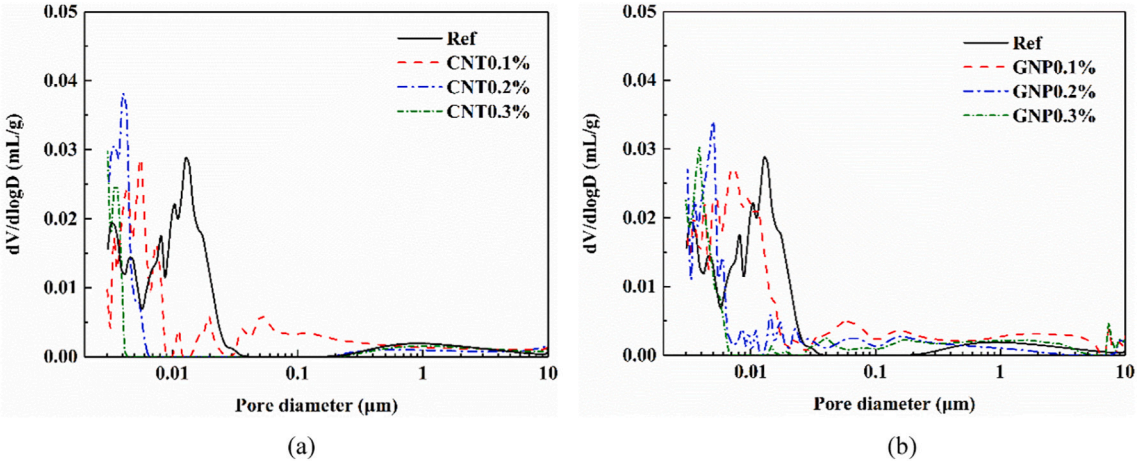

Fig. 4. Pore size distribution of UHPC mortar made with various (a) CNT and (b) GNP contents.

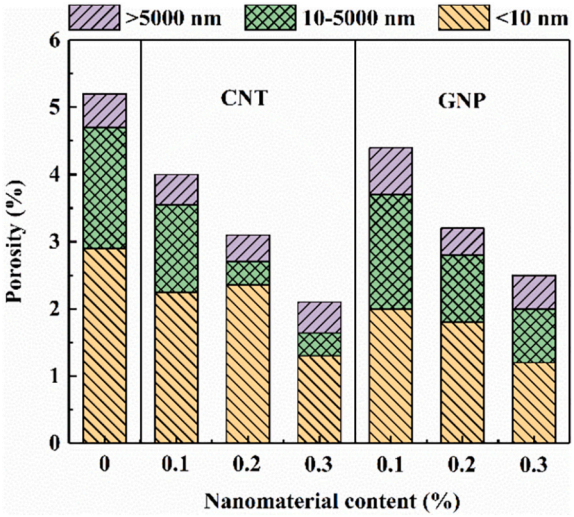

Fig. 5. Total porosity and the porosity of each type of pore for samples prepared with different nanomaterial contents.

approximately 5%. Such low total porosity is attributed to the optimized mixture proportioning and high fluidity of mixture that can reduce the entrapped air of hardened sample. The increase of nanomaterial content can lead to a reduction in total porosity. The total porosity was reduced to approximately 2.5% with the use of 0.3% nanomaterial.

Moreover, the use of nanomaterial was shown to decrease the porosities of capillary and gel pores. The increase of CNT content from 0 to 0.3% reduced the porosities of capillary and gel pores from 1.8% to 0.4% and from 2.9% to 1.3%, respectively. Such values were reduced to 0.8% and 1.2%, respectively, when 0.3% GNP was used. It is important to note that the proportion of gel pores was increased with the use of nanomaterial, given the reduced total porosity. This indicates a refinement in the pore structure, which is consistent with results reported in Fig. 4.

One of the mechanisms on the refinement in pore size and the decrease in porosity of UHPC mortar were associated with the transformation of porous $Ca(OH)_2$ to denser C-S-H gel [47]. Therefore, it can be deduced that the use of CNT and GNP enhanced the pozzolanic reactivity of SF and FAC, which increased the volume fraction of gel micro-pores. Moreover, CNT and GNP can act as nanofillers, thus decreasing the porosity of UHPC mortar [5,20,48]. It is important to note that CNT can lead to a lower porosity compared to that of GNP given a similar content. This is due to the fact that CNT has a greater specific surface area, resulting in more nucleation sites for C-S-H formation [21,43].

3.5. Nano-mechanical properties

Fig. 6 gives the typical load-depth curves of cement clinker, sand, and C-S-H of UHPC tested by nano-indentation. Cement clinker, sand, and C-S-H can be distinguished given the difference in achieved load-depth curves. A lower depth corresponds to a greater elastic modulus of phase given the constant test load. As shown in Fig. 6, the maximum depth of C-S-H ranged from 300 to 700 nm, corresponding to elastic modulus of from 10 to 60 GPa [29,30,32]. The indentation depths of C-S-H phases were greater than those of cement clinker and sand. This is due to the lower elastic moduli of C-S-H phases compared to those of clinker and sand.

The indentation modulus can be calculated as Eq. (1) [49]:

$$M = \frac{1}{2}\left(\frac{dp}{dh}\sqrt{\frac{\pi}{A}}\right)_{h=h_{max}} \quad (1)$$

where M is the indentation modulus; p and h are the indentation load and depth, respectively; h_{max} is the maximum indentation depth; A is the projected contact area that can be determined using the Oliver and Pharr's method [50].

The elastic modulus of tested phase is calculated by Eq. (2), given the indentation modulus and Poisson's ratio:

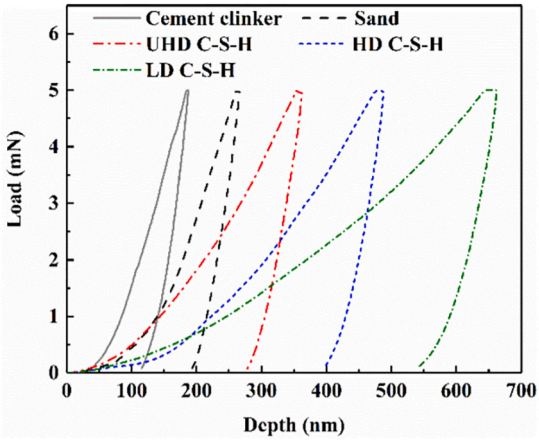

Fig. 6. Typical load-depth curves of cement clinker, sand, and C-S-H of UHPC tested by nano-indentation.

$$\frac{1}{M}=\frac{1-v^2}{E}+\frac{1-v_i^2}{E_i} \quad (2)$$

where E and v are the elastic modulus and Poisson's ratio of the tested phase, respectively; E_1 and v_1 are the elastic modulus and Poisson's ratio of the indentation tip, respectively.

The distribution of C-S-H elastic modulus for samples prepared with various nanomaterial contents are given in Fig. 7. In the figure, the position of the first column of 8 × 10 test grid is defined as 0 μm, and the average value of each column (8 nano-indentation points for each column) is reported. The clinker and sand that have elastic moduli greater than 60 GPa were excluded in averaging. It is important to note that high variations for the tested elastic moduli along different positions were observed for a given nanomaterial content. This is dependent on the highly variable nature of elastic modulus of C-S-H (including LD, HD, and UHD C-S-H) in UHPC, which can vary from 10 to 60 GPa [29,30,32]. For UHPC sample prepared without nanomaterial, the elastic modulus of C-S-H was around 28 GPa with the increase of distance relative to the first point. The addition of nanomaterial enhanced the elastic modulus. With additions of 0.1%, 0.2%, and 0.3% nanomaterials, the elastic moduli increased to approximately 31, 34, and 36 GPa, respectively.

Fig. 8 shows the proportions of LD, HD, and UHD C-S-H of UHPC samples prepared with different nanomaterial contents. The proportions of LD, HD, and UHD C-S-H are 36%, 51%, and 13%, respectively, for samples made without CNT and GNP. The use of nanomaterial can lead to higher HD and UHD C-S-H fractions. For example, the HD and UHD C-S-H proportions were enhanced to 65% and 23%, respectively, whereas the LD C-S-H proportion was decreased to 12% when CNT content increased from 0 to 0.3%. Such values of LD, HD, and UHD C-S-H proportions are 16%, 64%, and 20%, respectively, for UHPC prepared with 0.3% GNP. The increased proportions of HD and UHD C-S-H that have greater elastic moduli can therefore contribute to a greater mechanical strength.

3.6. ^{29}Si NMR

Fig. 9 shows the ^{29}Si NMR results of UHPC pastes made with various nanomaterial contents. In the spectra, Q represents the SiO_4 tetrahedron unit, and its superscript, n (n = 0, 1, 2, 3, and 4) corresponds to the number of tetrahedron units that are connected to Q. For example, Q^2 indicates that each SiO_4 tetrahedron unit connects with two adjacent SiO_4 tetrahedron units.

In general, the Q^0 at about −70 ppm represents the unhydrated cement clinker. For hydrated cement, the spectra mainly demonstrate signal peaks located at approximately −79, −83, and −85 ppm, corresponding to chain-end (Q^1), bridging (Q^2_b), and paired (Q^2_p) sites of C-S-H, respectively [51,52]. The Q^3 at about −97 ppm represents the cross-link of two C-S-H chains. The Q^4 at about −110 ppm represents the SF [29]. Moreover, the Al in cement and FAC, due to its pozzolanic reaction, can substitute for Si at bridging sites, resulting in the Q^2(1Al) and Q^3(1Al) at about −81 and −92 ppm, respectively [53].

Generally, a greater intensity of Q^2 and Q^3 signals indicate a higher hydration degree of cementitious materials, which can result in more C-S-H and greater polymerization degree. As shown in the reference spectrum of the figure, the intensity of Q^0 (−70 ppm) was significantly higher than that of Q^2 (−83 and −85 ppm). This indicates that a great portion of cement remains unhydrated for samples prepared without CNT and GNP. With the use of nanomaterial, the intensity of Q^0 decreased, and the intensity of Q^2 increased. The Q^2 intensity was greater than Q^0 when the nanomaterial content increased to 0.3%, indicating a significantly enhanced hydration degree with the use of nanomaterial.

The proportion of each Q^n specie can be quantitatively analyzed through deconvolution of the achieved spectra. Fig. 10 shows an example of deconvolution analysis of ^{29}Si NMR spectrum of reference UHPC mixture. The deconvolution was conducted by fitting the Gaussian peak profiles [54].

The ^{29}Si NMR spectra of samples prepared with different nanomaterial contents are deconvolved and given in Table 7. As shown in the table, the proportions of Q^0 and Q^1 decreased when the nanomaterial content increased from 0 to 0.3%. On the other hand, the proportions of Q^2 and Q^3 enhanced with the increase in nanomaterial content. It is important to mention that the Q^2 and Q^3 discussed in the paper include Q^2(1Al), Q^2_b, Q^2_p, and Q^3(1Al). This indicates that the addition of CNT and GNP can promote the transformation from Q^0 and Q^1 to Q^2 and Q^3, leading to an enhanced polymerization degree of C-S-H chains. Such enhancement in polymerization degree can be due to the improved cement hydration with the use of CNT and GNP. Moreover, as reported in [55,56], the electronegative CNT and GNP can attract Ca^{2+} and repel $Al(OH)_4^-$, leading to the redistribution of elements. This can increase the polymerization degree of C-S-H. The enhanced polymerization degree can therefore increase the fractions of HD and UHD C-S-H, contributing to the improved mechanical properties.

As shown in the table, the proportion of Q^2(1Al) is obviously greater than that of Q^2_b for a given nanomaterial content. This is attributed to the fact that a majority of bridging sites of C-S-H can be occupied by Al

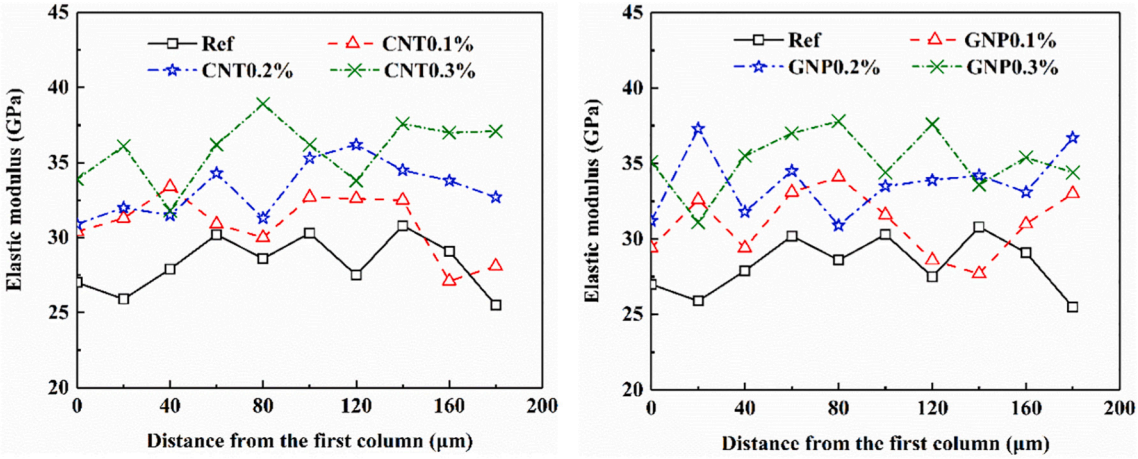

Fig. 7. C-S-H elastic modulus distribution for samples made with various (a) CNT and (b) GNP contents determined from nano-indentation.

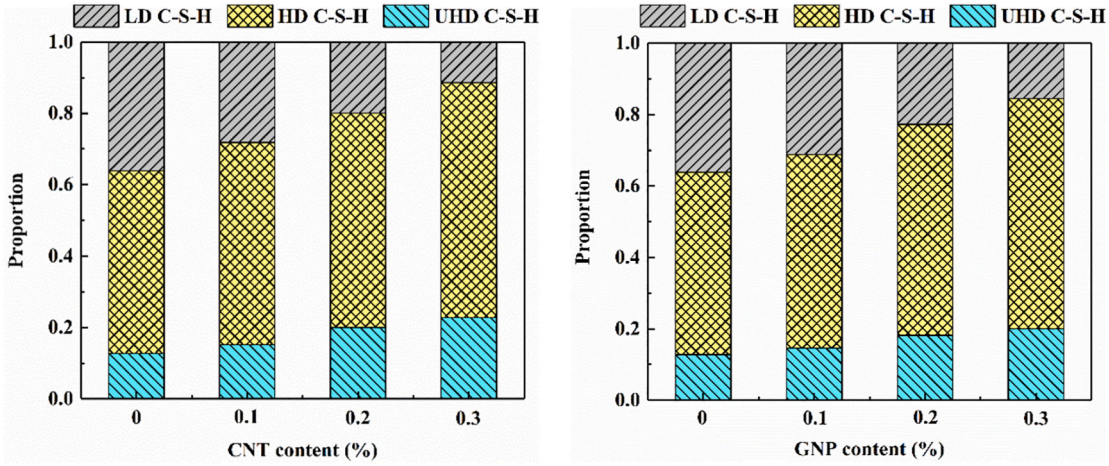

Fig. 8. Proportions of each type of C-S-H for samples prepared with various contents of (a) CNT and (b) GNP.

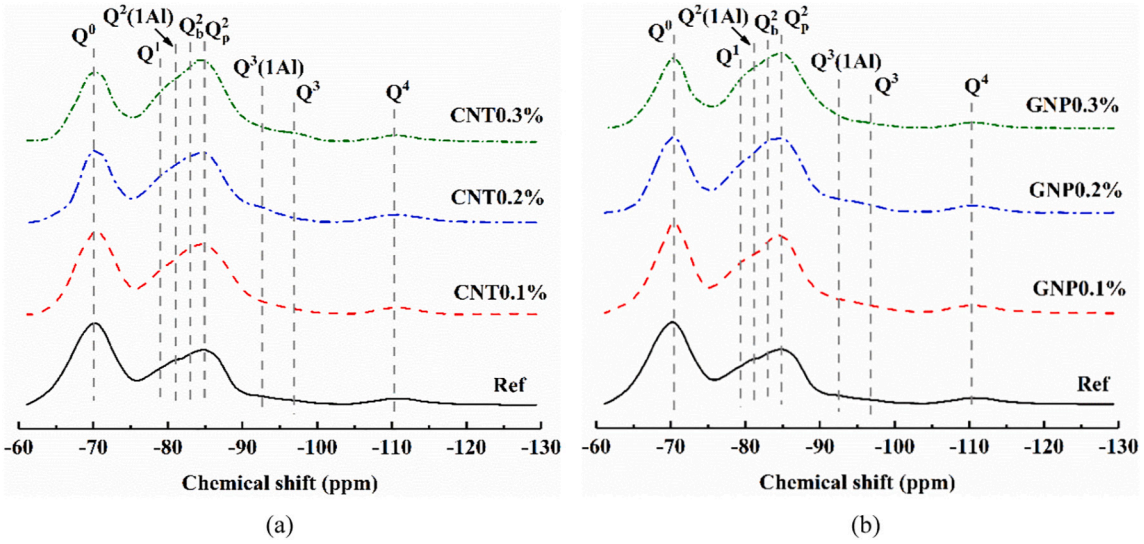

Fig. 9. ^{29}Si NMR spectra of samples prepared with various (a) CNT and (b) GNP contents.

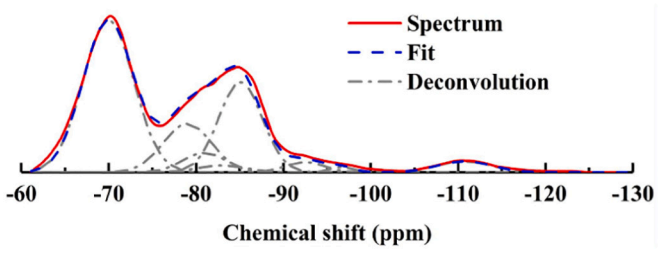

Fig. 10. Deconvolution analysis of ^{29}Si NMR spectrum (Ref).

rather than Si when supplementary cementitious materials are used at a high content [53,57,58]. Furthermore, the proportions of $Q^2(1Al)$ and $Q^3(1Al)$ significantly increased with the use of CNT and GNP. This means that CNT and GNP can favor the substitution of Si by Al. In addition, the changes in CNT and GNP content resulted in various Al-coordination environments, i.e., tetra-, penta-, and hexa-coordinated Al species, noted as Al(IV), Al(V), and Al(VI), respectively, in hydration products of UHPC [59,60], which is elaborated further in Section 3.7 with ^{27}Al NMR results.

The mean chain length (MCL), defined as the average number of aluminosilicate tetrahedra per C-S-H chain, is used to assess the polymerization degree of C-S-H [51]. The MCL of cross-linked C-S-H can be calculated by Eq. (3) [61]:

$$\mathrm{MCL} = \frac{4\left[\mathrm{Q}^1 + \mathrm{Q}^2 + \mathrm{Q}^2(1\mathrm{Al}) + \mathrm{Q}^3 + 2\mathrm{Q}^3(1\mathrm{Al})\right]}{\mathrm{Q}^1} \quad (3)$$

Fig. 11 shows the variations in MCL values with different nanomaterial contents. For the reference sample prepared without nanomaterial, the MCL value is approximately 13. The addition of nanomaterial can enhance the MCL value. The use of 0.3% CNT and GNP led to a 140% and 110% greater MCL values, respectively, compared to that of reference sample. As concluded from Table 7, CNT and GNP can facilitate the transformation from Q^0 and Q^1 to Q^2 and Q^3, hence enhancing the polymerization degree of C-S-H. On the other hand, CNT can lead to a longer MCL compared to that of GNP, for a given content, which is consistent with the mechanical and MIP results.

Table 7
Deconvolution of ^{29}Si NMR results of samples prepared with different nanomaterial contents (%).

Nanomaterial content	Q^0	Q^1	$Q^2(1Al)$	Q^2_b	Q^2_p	$Q^3(1Al)$	Q^3	Q^4
Ref	48.3	15.8	5.7	2.0	19.8	3.1	1.8	3.5
CNT0.1%	43.1	13.9	6.8	2.8	24.8	3.6	2.1	2.9
CNT0.2%	37.6	10.7	8.1	3.9	30.9	4.3	2.3	2.2
CNT0.3%	32.4	9.1	9.6	5.2	34.2	5.0	2.7	1.8
GNP0.1%	43.7	14.5	6.6	2.6	23.8	3.4	2.3	3.1
GNP0.2%	38.4	11.7	7.8	3.7	29.4	3.9	2.6	2.5
GNP0.3%	33.5	10.2	8.9	5.3	32.8	4.5	2.8	1.7

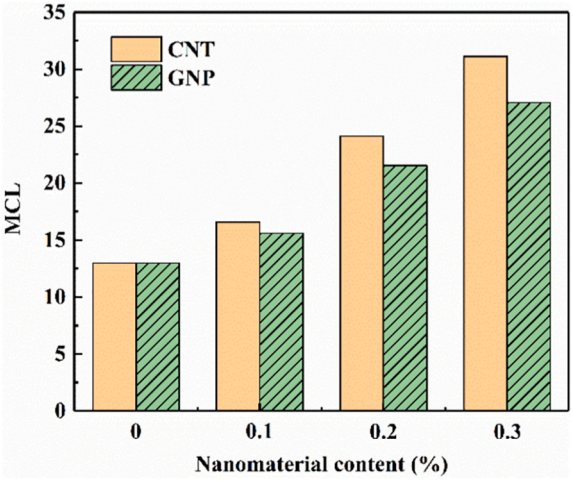

Fig. 11. Variations in MCL values with different nanomaterial contents.

3.7. ^{27}Al NMR

The ^{27}Al NMR results of UHPC pastes prepared with various nanomaterial contents are shown in Fig. 12. Three distinct Al-coordination environments, i.e., Al(IV), Al(V), and Al(VI), with corresponding chemical shifts at 50–80 ppm, 30–50 ppm, and 0–20 ppm, respectively, were observed [62,63]. The signal peak centered at 60 ppm corresponded to the Al(IV) in C-S-H ($Q^2(1Al)$ and $Q^3(1Al)$) [60,62,63]. A much lower signal between 30 and 50 ppm is associated with Al(V) in the interlayer sites of C-S-H structures [62]. It is important to mention that the Al—Si substitution (i.e., $Q^2(1Al)$ and $Q^3(1Al)$) can introduce negative charges, which are balanced by interlayer Ca^{2+} and Al(V) [64].

As shown in the figure, the signal intensity at chemical shift from 30 to 80 ppm increased with the enhancement in CNT and GNP content. This indicates that the use of CNT and GNP can lead to an elevated degree of Al—Si substitution. Such increased Al—Si substitution also necessitate more Al(V) to balance the introduced negative charges. This is well consistent with ^{29}Si NMR results where a higher CNT and GNP content is found to enhance the proportions of $Q^2(1Al)$ and $Q^3(1Al)$.

The signal centered at 10 ppm corresponded to the Al(VI) of AFm (Al_2O_3-Fe_2O_3-mono) [62], and a small shoulder at chemical shift from 0 to 5 ppm is due to the formation of amorphous aluminate hydrate (third aluminate hydrate, TAH) [59,65]. On the other hand, no signal corresponding to ettringite at 12.5 ppm was observed. Thermodynamic modelling carried out in [28] indicated that the ettringite can be unstable when fly ash was used at replacement ratio (of cement) greater than 40%. Other minerals, such as strätlingite may form with the use of high-volume Al-rich fly ash, depending on the reactivity and Al_2O_3 content of the fly ash as well as the uptake of Al in C-S-H.

3.8. BSE-EDX

As concluded from Sections 3.6 and 3.7, the addition of CNT and GNP can increase the polymerization degree and Al(IV) substitution for Si of C-S-H, thus influencing the composition and structure of C-S-H. The variations in Ca/Si and Al/Si, caused by the use of the two nanomaterials can be quantitatively evaluated through the BSE-EDX analysis.

Fig. 13 shows a typical sample used for the BSE-EDX analysis. River sand, LWS, clinker, FAC, and C-S-H can be clearly distinguished from the BSE image. For each sample, at least 100 EDX analysis spots that contain atomic percentages of Ca, Si, and Al were randomly collected. River sand, LWS, clinker, and FAC were avoided for EDX spots collection.

The variations of Ca/Si and Al/Si of samples prepared with different nanomaterial contents are shown in Fig. 14. Regardless of CNT and GNP content, the Ca/Si values ranged from 0.5 to 3.5. The majority of Ca/Si

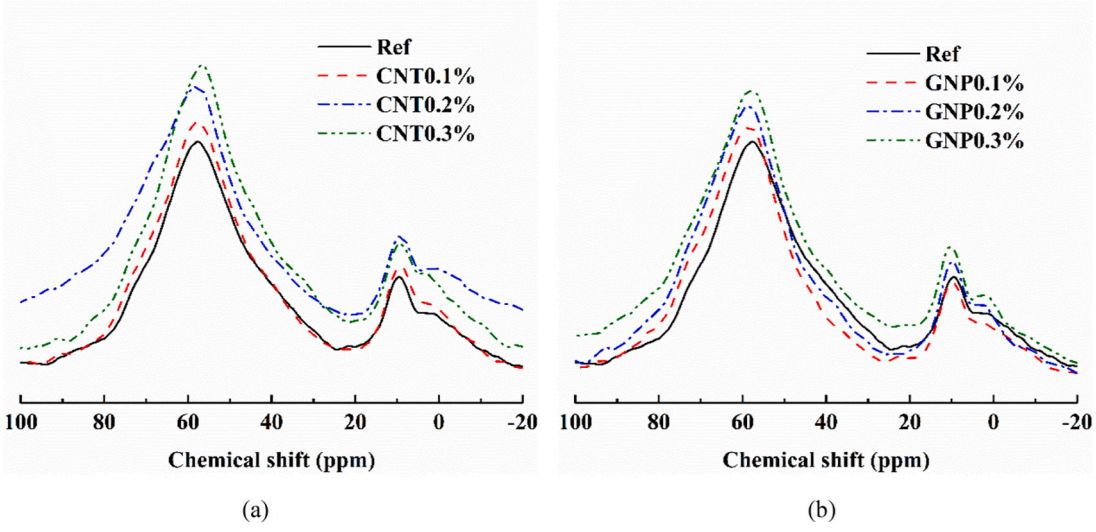

Fig. 12. ^{27}Al NMR spectra of samples made with various (a) CNT and (b) GNP contents.

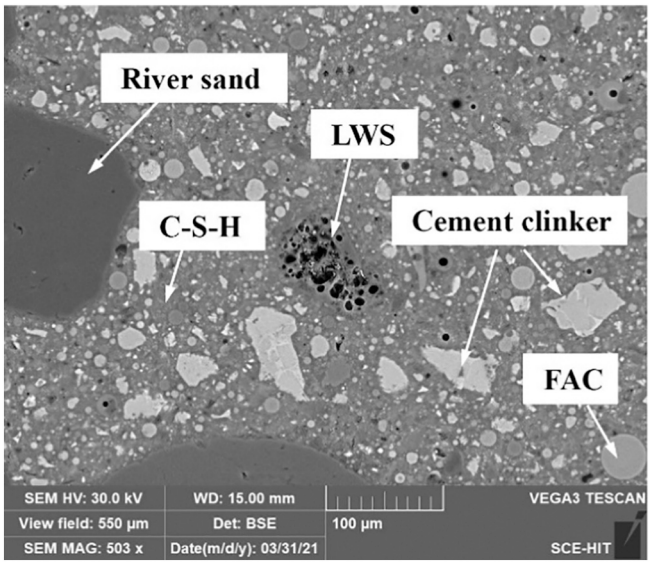

Fig. 13. A typical BSE-EDX sample (Ref).

values were 1.5–2.5, which is consistent with the results reported in [29,66]. For samples made without nanomaterial, the average Ca/Si and Al/Si values can be on the order of 2.25 and 0.1, respectively. With the increase in CNT and GNP content, the average Ca/Si and Al/Si values were shown to decrease and increase, respectively. When the nanomaterial content increased from 0 to 0.3%, the average Ca/Si and Al/Si were on the order of 1.75 and 0.15, respectively.

In general, a lower Ca/Si indicates a higher polymerization degree of C-S-H accompanied with longer chains [29,67]. Due to the enhanced cement hydration and redistribution of elements (Ca^{2+} and $Al(OH)_4^-$) with the use of CNT and GNP, the polymerization degree and the MCL increased with the nanomaterial content. This can result in a reduced Ca/Si. Moreover, the addition of CNT and GNP can favor the Al(IV) substitution for Si, as concluded in Section 3.7. Such Al—Si substitution can lead to increased Al/Si [28,57,58].

The NMR and BSE-EDX results confirmed that the nano-structure and composition of C-S-H were influenced by CNT and GNP through increasing MCL (polymerization degree) and Al—Si substitution. The enhanced MCL can lead to a lower Ca/Si value. In addition, the increased Al—Si substitution increased the Al/Si of C-S-H, indicating an enhanced pozzolanic reaction of FAC. This reduced the pH value of pore solution ($Ca(OH)_2$ consumption), leading to the destabilization of ettringite. In this case, strätlingite may form given the use of high-volume Al-rich fly ash.

3.9. Evolutions in composition and structure of C-S-H

As pointed out in Section 3.8, the use of CNT and GNP can lead to a decreased Ca/Si and an increased Al/Si. This can therefore affect the composition and structure of C-S-H. This section aims to investigate the evolutions in the composition and structure of C-S-H due to changes of Ca/Si and Al/Si that are caused by the use of CNT and GNP.

It is acknowledged that the nano-structure of C-S-H is similar to that of tobermorite. Fig. 15 shows the nano-structure of a 14 Å tobermorite that is reported in the American Mineralogist Crystal Structure Database [68]. The silicate chains in the tobermorite are structured according to the "dreierketten model" [32,69,70]. In this model, the silicate chains are flanked by a Ca—O layer and a hydrous layer. Ca_I and Ca_{II} refer to the intralayer and interlayer Ca atoms, respectively. It is important to mention that the chemical bonds between Ca and O atoms are not shown in the figure. Each silicate tetrahedron shares two O atoms with two adjacent silicate tetrahedrons, corresponding to Q^2 species as pointed out in Section 3.6. Generally, the silicate chains in the original tobermorite are infinite, corresponding to a Ca/Si of 0.83.

The cement generally contains a great content of CaO. In this case, Ca can substitute for the silicate tetrahedron (noted as Ca_B) during cement hydration, breaking the idealized infinite silicate chains into finite segments [71], as illustrated in Fig. 16. The segments are terminated by Q^1 species. Such substitutions can introduce negative charges that are balance by additional Ca (noted as Ca_C) and OH^-. The increase in Ca substitution for silicate tetrahedron necessitates more Ca_C and OH^- to secure a balanced charge. Moreover, such increased Ca substitution can result in a greater number of C-S-H segments that have shorter chain length. This can lead to a reduced MCL and an enhanced Ca/Si of C-S-H.

In addition, Al in the hydration system, most of which comes from the SCMs (e.g., FAC) can substitute for Si in C-S-H, leading to the formation of aluminate tetrahedron [28]. Such Al in the aluminate tetrahedron corresponds to the Al(IV), as pointed out in Section 3.7. In the case of this paper, it can be deduced that both Ca substitution for silicate tetrahedron and Al substitution for Si occurred in the C-S-H, as illustrated in Fig. 17. It is important to note that Al—Si substitution will not break up the C-S-H chain. Similarly, the Al—Si substitution necessitates additional Ca_C and OH^- to keep a balanced charge.

As concluded from Section 3.8, the addition of CNT and GNP can lead to a reduced Ca/Si and an increased Al/Si. The reduced Ca/Si indicates

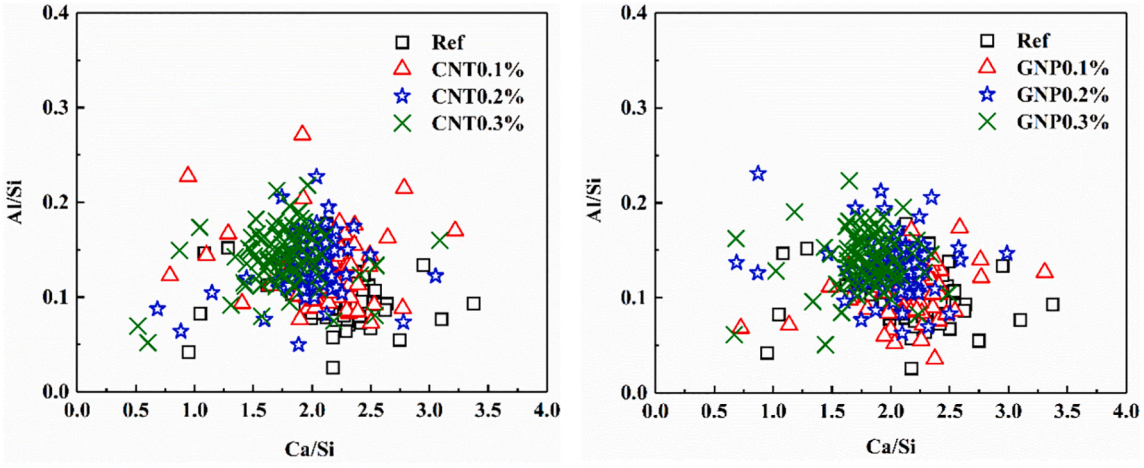

Fig. 14. Variations of Ca/Si and Al/Si of samples made with various (a) CNT and (b) GNP contents.

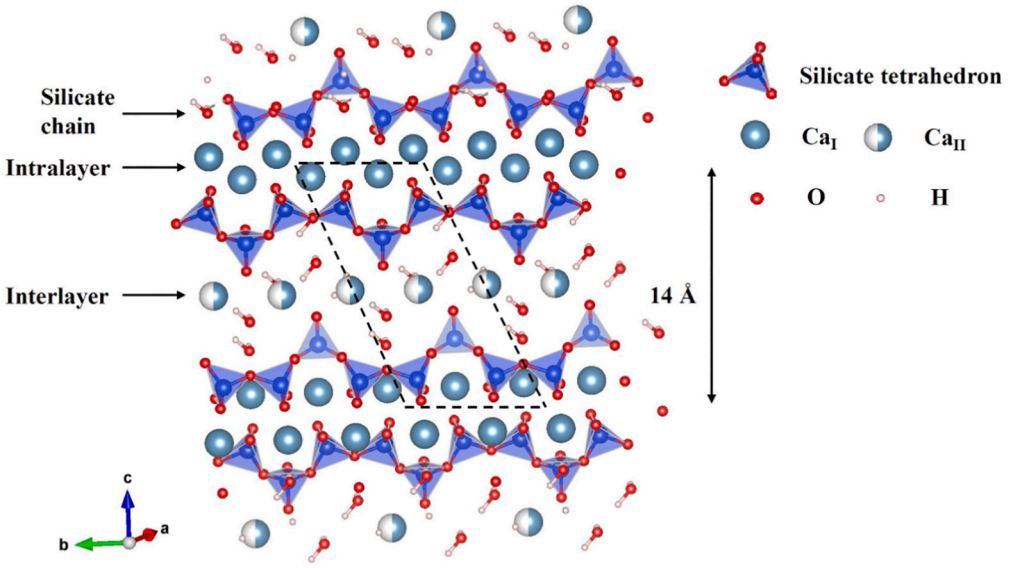

Fig. 15. Nano-structure of a layered 14 Å tobermorite (Ca/Si = 0.83) corresponding to the "dreierketten model".

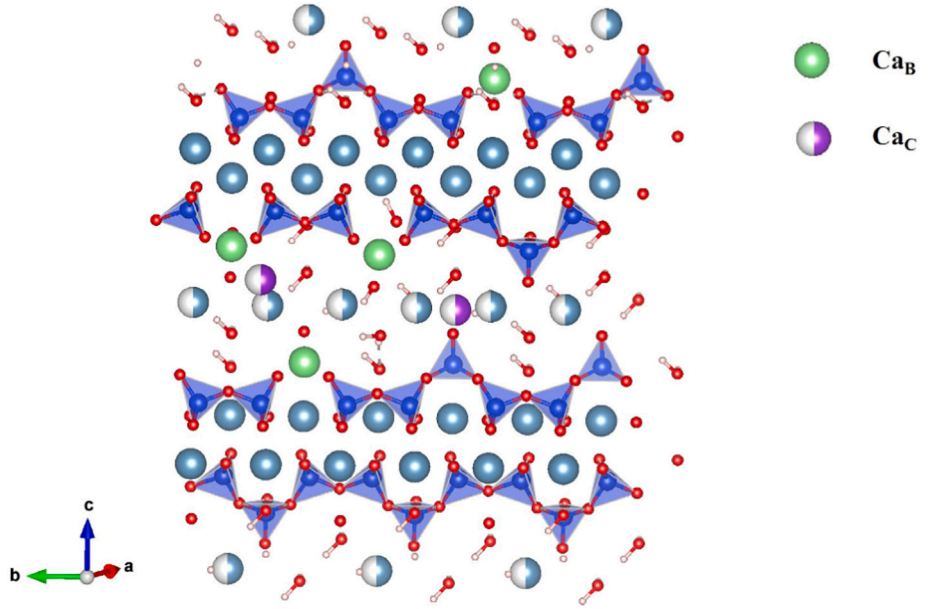

Fig. 16. Illustration of Ca substitution for silicate tetrahedrons.

that more silicate tetrahedrons are connected to the C-S-H chain segments. Moreover, the substitution of Ca for silicate tetrahedron is relatively decreased. This can enhance the chain lengths of C-S-H segments, leading to an increased MCL, which is in agreement with the results shown in Fig. 11. On the other hand, the increased Al/Si indicates an elevated degree of Al—Si substitution. Although the Al—Si substitution are shown to have no significant influence on the MCL of C-S-H, the increase of such substitution can lead to more Ca_C and OH^- to keep charge-balanced.

4. Conclusions

In this paper, the effect of carbon nanotube (CNT) and graphite nanoplatelet (GNP) on composition, structure, and nano-mechanical characteristics of C-S-H in UHPC was investigated. The non-proprietary UHPC was proportioned with 17% lightweight sand for internal curing. The CNT and GNP content ranged from 0 to 0.3%, by mass of binder. The hydration kinetics, mechanical properties, and pore structure were determined. Based on the findings, the following conclusions can be drawn:

1. The addition of 0–0.1% CNT or GNP reduced plastic viscosity of UHPC due to the filling effect of nanomaterials. Further increase in nanomaterial content to 0.3% resulted in 5 Pa·s increase in plastic viscosity.
2. The addition of 0.3% CNT or GNP enhanced the peak heat flow and cumulative heat by 15% and 35%–45%, respectively, given the nucleation effect of the nanomaterial.
3. The use of 0.3% CNT or GNP led to approximately 20 MPa increase in compressive strengths of non-fibrous UHPC mortar and fibrous UHPC (2% steel fibers), compared to those made without any nanomaterial. Such enhancement is attributed to the refined pore structure (total porosity of 2.5% vs. 5%).

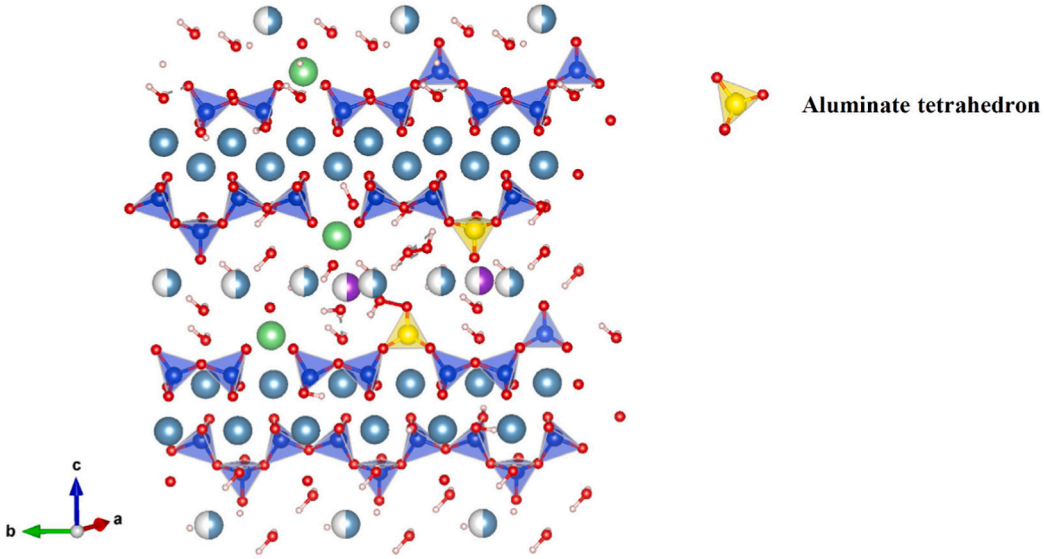

Fig. 17. Illustration of Ca substitution for silicate tetrahedrons and Al substitution for Si.

4. The mean elastic modulus of C-S-H determined from nano-indentation increased from 28 to 34 GPa with the use of 0.3% CNT or GNP. The proportion of high density and ultra-high density C-S-H that have greater elastic moduli relative to that of low density C-S-H increased from 65% and 90% with the use of 0.3% nanomaterials.
5. Q^n, which is used to evaluate the connectivity of SiO_4 tetrahedron units of C-S-H chain was found to transform from Q^0 and Q^1 to Q^2 and Q^3 with the use of CNT and GNP, leading to longer mean chain length (MCL) of the C-S-H. The MCL was increased by 140% and 110% with the use of 0.3% CNT and GNP, respectively.
6. The increase in CNT and GNP content from 0 to 0.3% resulted in a reduced Ca/Si of C-S-H from 2.25 to 1.75. Moreover, the use of CNT and GNP increased the Al/Si of C-S-H from 0.1 to 0.15, indicating greater pozzolanic reactivity of the fly ash.
7. Given the greater specific surface area of CNT compared to GNP, the use of CNT can provide more nucleation sites for C-S-H formation compared to GNP. Therefore, samples prepared with CNT showed a longer MCL, lower porosity, larger proportion of HD and UHD C-S-H, higher hydration rate, and greater strength compared to those prepared with similar GNP content.

CRediT authorship contribution statement

Huanghuang Huang: Investigation, Validation, Writing - Original Draft; *Le Teng*: Investigation, Writing - Review & Editing; *Xiaojian Gao*: Conceptualization, Methodology, Data Curation, Funding acquisition, Writing - Review & Editing; *Kamal H. Khayat*: Conceptualization, Resources, Funding acquisition, Supervision, Writing - Review & Editing; *Fazhou Wang*: Methodology, Supervision, Writing - Review & Editing; *Zhichao Liu*: Methodology, Writing - Review & Editing.

Declaration of competing interest

The authors declare that they have no known competing financial interests or personal relationships that could have appeared to influence the work reported in this paper.

Acknowledgment

This work was supported by the Clayco Advanced Construction and Material Laboratory (ACML) of the Center for Infrastructure Engineering Studies (CIES) and the National Natural Science Foundation of China (grant number: U2106220).

References

[1] K.M. Liew, M.F. Kai, L.W. Zhang, Carbon nanotube reinforced cementitious composites: an overview, Compos. A: Appl. Sci. Manuf. 91 (2016) 301–323, https://doi.org/10.1016/j.compositesa.2016.10.020.
[2] W. Dong, W. Li, X. Zhu, D. Sheng, S.P. Shah, Multifunctional cementitious composites with integrated self-sensing and hydrophobic capacities toward smart structural health monitoring, Cem. Concr. Compos. 118 (2021), 103962, https://doi.org/10.1016/j.cemconcomp.2021.103962.
[3] D. Gao, M. Sturm, Y.L. Mo, Electrical resistance of carbon-nanofiber concrete, Smart Mater. Struct. 18 (2009) 95039.
[4] S. Park, R.S. Ruoff, Chemical methods for the production of graphenes, Nat. Nanotechnol. 4 (2009) 217–224, https://doi.org/10.1038/nnano.2009.58.
[5] B. Han, S. Sun, S. Ding, L. Zhang, X. Yu, J. Ou, Review of nanocarbon-engineered multifunctional cementitious composites, Compos. A: Appl. Sci. Manuf. 70 (2015) 69–81, https://doi.org/10.1016/j.compositesa.2014.12.002.
[6] T. Belytschko, S.P. Xiao, G.C. Schatz, R.S. Ruoff, Atomistic simulations of nanotube fracture, Phys. Rev. B 65 (2002), 235430, https://doi.org/10.1103/PhysRevB.65.235430.
[7] F. de Larrard, T. Sedran, Optimization of ultra-high-performance concrete by the use of a packing model, Cem. Concr. Res. 24 (1994) 997–1009, https://doi.org/10.1016/0008-8846(94)90022-1.
[8] K. Habel, M. Viviani, E. Denarié, E. Brühwiler, Development of the mechanical properties of an ultra-high performance fiber reinforced concrete (UHPFRC), Cem. Concr. Res. 36 (2006) 1362–1370, https://doi.org/10.1016/j.cemconres.2006.03.009.
[9] K.H. Khayat, W. Meng, K. Vallurupalli, L. Teng, Rheological properties of ultra-high-performance concrete — an overview, Cem. Concr. Res. 124 (2019), 105828, https://doi.org/10.1016/j.cemconres.2019.105828.
[10] W. Meng, K.H. Khayat, Mechanical properties of ultra-high-performance concrete enhanced with graphite nanoplatelets and carbon nanofibers, Compos. Part B 107 (2016) 113–122, https://doi.org/10.1016/j.compositesb.2016.09.069.
[11] P. Richard, M. Cheyrezy, Composition of reactive powder concretes, Cem. Concr. Res. 25 (1995) 1501–1511, https://doi.org/10.1016/0008-8846(95)00144-2.
[12] C. Shi, Z. Wu, J. Xiao, D. Wang, Z. Huang, Z. Fang, A review on ultra high performance concrete: part I. Raw materials and mixture design, Constr. Build. Mater. 101 (2015) 741–751, https://doi.org/10.1016/j.conbuildmat.2015.10.088.
[13] H. Huang, X. Gao, L. Li, H. Wang, Improvement effect of steel fiber orientation control on mechanical performance of UHPC, Constr. Build. Mater. 188 (2018), https://doi.org/10.1016/j.conbuildmat.2018.08.146.
[14] H. Huang, X. Gao, A. Zhang, Numerical simulation and visualization of motion and orientation of steel fibers in UHPC under controlling flow condition, Constr. Build. Mater. 199 (2019) 624–636, https://doi.org/10.1016/j.conbuildmat.2018.12.055.
[15] Z. Wu, C. Shi, K.H. Khayat, S. Wan, Effects of different nanomaterials on hardening and performance of ultra-high strength concrete (UHSC), Cem. Concr. Compos. 70 (2016) 24–34, https://doi.org/10.1016/j.cemconcomp.2016.03.003.
[16] Z. Wu, K.H. Khayat, C. Shi, Effect of nano-SiO_2 particles and curing time on development of fiber-matrix bond properties and microstructure of ultra-high strength concrete, Cem. Concr. Res. 95 (2017) 247–256, https://doi.org/10.1016/j.cemconres.2017.02.031.
[17] S. Kawashima, K. Wang, R.D. Ferron, J.H. Kim, N. Tregger, S. Shah, A review of the effect of nanoclays on the fresh and hardened properties of cement-based

materials, Cem. Concr. Res. 147 (2021), 106502, https://doi.org/10.1016/j.cemconres.2021.106502.
[18] X. Cui, B. Han, Q. Zheng, X. Yu, S. Dong, L. Zhang, J. Ou, Mechanical properties and reinforcing mechanisms of cementitious composites with different types of multiwalled carbon nanotubes, Compos. A: Appl. Sci. Manuf. 103 (2017) 131–147, https://doi.org/10.1016/j.compositesa.2017.10.001.
[19] H. Du, H.J. Gao, S.D. Pang, Improvement in concrete resistance against water and chloride ingress by adding graphene nanoplatelet, Cem. Concr. Res. 83 (2016) 114–123, https://doi.org/10.1016/j.cemconres.2016.02.005.
[20] T. Nochaiya, A. Chaipanich, Behavior of multi-walled carbon nanotubes on the porosity and microstructure of cement-based materials, Appl. Surf. Sci. 257 (2011) 1941–1945, https://doi.org/10.1016/j.apsusc.2010.09.030.
[21] M.S. Konsta-Gdoutos, Z.S. Metaxa, S.P. Shah, Highly dispersed carbon nanotube reinforced cement based materials, Cem. Concr. Res. 40 (2010) 1052–1059, https://doi.org/10.1016/j.cemconres.2010.02.015.
[22] R. Qin, A. Zhou, Z. Yu, Q. Wang, D. Lau, Role of carbon nanotube in reinforcing cementitious materials: an experimental and coarse-grained molecular dynamics study, Cem. Concr. Res. 147 (2021), 106517, https://doi.org/10.1016/j.cemconres.2021.106517.
[23] M.S. Konsta-Gdoutos, Z.S. Metaxa, S.P. Shah, Multi-scale mechanical and fracture characteristics and early-age strain capacity of high performance carbon nanotube/cement nanocomposites, Cem. Concr. Compos. 32 (2010) 110–115, https://doi.org/10.1016/j.cemconcomp.2009.10.007.
[24] A. Peyvandi, L.A. Sbia, P. Soroushian, K. Sobolev, Effect of the cementitious paste density on the performance efficiency of carbon nanofiber in concrete nanocomposite, Constr. Build. Mater. 48 (2013) 265–269, https://doi.org/10.1016/j.conbuildmat.2013.06.094.
[25] Z. Chen, J.L.G. Lim, E.H. Yang, Ultra high performance cement-based composites incorporating low dosage of plasma synthesized carbon nanotubes, Mater. Des. 108 (2016) 479–487, https://doi.org/10.1016/j.matdes.2016.07.016.
[26] J.E. Rossen, B. Lothenbach, K.L. Scrivener, Composition of C-S-H in pastes with increasing levels of silica fume addition, Cem. Concr. Res. 75 (2015) 14–22, https://doi.org/10.1016/j.cemconres.2015.04.016.
[27] J. Haas, A. Nonat, From C-S-H to C-A-S-H: experimental study and thermodynamic modelling, Cem. Concr. Res. 68 (2015) 124–138, https://doi.org/10.1016/j.cemconres.2014.10.020.
[28] B. Lothenbach, K. Scrivener, R.D. Hooton, Supplementary cementitious materials, Cem. Concr. Res. 41 (2011) 1244–1256, https://doi.org/10.1016/j.cemconres.2010.12.001.
[29] P. Shen, L. Lu, Y. He, F. Wang, S. Hu, The effect of curing regimes on the mechanical properties, nano-mechanical properties and microstructure of ultra-high performance concrete, Cem. Concr. Res. 118 (2019) 1–13, https://doi.org/10.1016/j.cemconres.2019.01.004.
[30] P. Mondal, S.P. Shah, L. Marks, A reliable technique to determine the local mechanical properties at the nanoscale for cementitious materials, Cem. Concr. Res. 37 (2007) 1440–1444, https://doi.org/10.1016/j.cemconres.2007.07.001.
[31] M. Vandamme, F.J. Ulm, P. Fonollosa, Nanogranular packing of C-S-H at substochiometric conditions, Cem. Concr. Res. 40 (2010) 14–26, https://doi.org/10.1016/j.cemconres.2009.09.017.
[32] E.M. Foley, J.J. Kim, M.M. Reda Taha, Synthesis and nano-mechanical characterization of calcium-silicate-hydrate (C-S-H) made with 1.5 CaO/SiO_2 mixture, Cem. Concr. Res. 42 (2012) 1225–1232, https://doi.org/10.1016/j.cemconres.2012.05.014.
[33] W. Meng, K.H. Khayat, Effect of graphite nanoplatelets and carbon nanofibers on rheology, hydration, shrinkage, mechanical properties, and microstructure of UHPC, Cem. Concr. Res. 105 (2018) 64–71, https://doi.org/10.1016/j.cemconres.2018.01.001.
[34] M.O. Mohsen, R. Taha, A. Abu Taqa, A. Shaat, Optimum carbon nanotubes' content for improving flexural and compressive strength of cement paste, Constr. Build. Mater. 150 (2017) 395–403, https://doi.org/10.1016/j.conbuildmat.2017.06.020.
[35] A. Peyvandi, P. Soroushian, N. Abdol, A.M. Balachandra, Surface-modified graphite nanomaterials for improved reinforcement efficiency in cementitious paste, Carbon N. Y. 63 (2013) 175–186, https://doi.org/10.1016/j.carbon.2013.06.069.
[36] W. Meng, M. Valipour, K.H. Khayat, Optimization and performance of cost-effective ultra-high performance concrete, Mater. Struct. 50 (2016) 29, https://doi.org/10.1617/s11527-016-0896-3.
[37] G. Constantinides, F.-J. Ulm, The effect of two types of C-S-H on the elasticity of cement-based materials: results from nanoindentation and micromechanical modeling, Cem. Concr. Res. 34 (2004) 67–80, https://doi.org/10.1016/S0008-8846(03)00230-8.
[38] Z. Pi, H. Xiao, R. Liu, M. Liu, H. Li, Effects of brass coating and nano-SiO_2 coating on steel fiber–matrix interfacial properties of cement-based composite, Compos. Part B 189 (2020), 107904, https://doi.org/10.1016/j.compositesb.2020.107904.
[39] S. Jiang, B. Shan, J. Ouyang, W. Zhang, X. Yu, P. Li, B. Han, Rheological properties of cementitious composites with nano/fiber fillers, Constr. Build. Mater. 158 (2018) 786–800, https://doi.org/10.1016/j.conbuildmat.2017.10.072.
[40] M. Jung, Y.Soon Lee, S.G. Hong, J. Moon, Carbon nanotubes (CNTs) in ultra-high performance concrete (UHPC): dispersion, mechanical properties, and electromagnetic interference (EMI) shielding effectiveness (SE), Cem. Concr. Res. 131 (2020), 106017, https://doi.org/10.1016/j.cemconres.2020.106017.
[41] K.H. Khayat , Workability, testing, and performance of self-consolidating concrete, ACI Mater. J. 96 (n.d.). doi:10.14359/632.
[42] K. Wille, K.J. Loh, Nanoengineering ultra-high-performance concrete with multiwalled carbon nanotubes, Transp. Res. Rec. 2142 (2010) 119–126.
[43] H. Du, S.D. Pang, Enhancement of barrier properties of cement mortar with graphene nanoplatelet, Cem. Concr. Res. 76 (2015) 10–19, https://doi.org/10.1016/j.cemconres.2015.05.007.
[44] J. Cheung, A. Jeknavorian, L. Roberts, D. Silva, Impact of admixtures on the hydration kinetics of Portland cement, Cem. Concr. Res. 41 (2011) 1289–1309, https://doi.org/10.1016/j.cemconres.2011.03.005.
[45] K.L. Scrivener, P. Juilland, P.J.M. Monteiro, Advances in understanding hydration of Portland cement, Cem. Concr. Res. 78 (2015) 38–56, https://doi.org/10.1016/j.cemconres.2015.05.025.
[46] J. Liu, N. Farzadnia, C. Shi, Microstructural and micromechanical characteristics of ultra-high performance concrete with superabsorbent polymer (SAP), Cem. Concr. Res. 149 (2021), 106560, https://doi.org/10.1016/j.cemconres.2021.106560.
[47] L. Wang, N. Ur Rehman, I. Curosu, Z. Zhu, M.A.B. Beigh, M. Liebscher, L. Chen, D. C.W. Tsang, S. Hempel, V. Mechtcherine, On the use of limestone calcined clay cement (LC3) in high-strength strain-hardening cement-based composites (HS-SHCC), Cem. Concr. Res. 144 (2021), 106421, https://doi.org/10.1016/j.cemconres.2021.106421.
[48] J.M. Makar, G.W. Chan, Growth of cement hydration products on single-walled carbon nanotubes, J. Am. Ceram. Soc. 92 (2009) 1303–1310, https://doi.org/10.1111/j.1551-2916.2009.03055.x.
[49] L. Sorelli, G. Constantinides, F.J. Ulm, F. Toutlemonde, The nano-mechanical signature of ultra high performance concrete by statistical nanoindentation techniques, Cem. Concr. Res. 38 (2008) 1447–1456, https://doi.org/10.1016/j.cemconres.2008.09.002.
[50] W.C. Oliver, G.M. Pharr, An improved technique for determining hardness and elastic modulus using load and displacement sensing indentation experiments, J. Mater. Res. 7 (1992) 1564–1583, https://doi.org/10.1557/JMR.1992.1564.
[51] R.J. Myers, E. L'Hôpital, J.L. Provis, B. Lothenbach, Effect of temperature and aluminium on calcium (alumino)silicate hydrate chemistry under equilibrium conditions, Cem. Concr. Res. 68 (2015) 83–93, https://doi.org/10.1016/j.cemconres.2014.10.015.
[52] J. Skibsted, M.D. Andersen, The effect of alkali ions on the incorporation of aluminum in the calcium silicate hydrate (C–S–H) phase resulting from Portland cement hydration studied by ^{29}Si MAS NMR, J. Am. Ceram. Soc. 96 (2013) 651–656, https://doi.org/10.1111/jace.12024.
[53] N.K. Lee, K.T. Koh, M.O. Kim, G.S. Ryu, Uncovering the role of micro silica in hydration of ultra-high performance concrete (UHPC), Cem. Concr. Res. 104 (2018) 68–79, https://doi.org/10.1016/j.cemconres.2017.11.002.
[54] G. Engelhardt, D. Michel, High-Resolution Solid-State NMR of Silicates and Zeolites, John Wiley Sons New York Ny, 1987.
[55] Z. Li, X. Shi, Graphene oxide modified, clinker-free cementitious paste with principally alkali-activated fly ash, Fuel 269 (2020), 117418, https://doi.org/10.1016/j.fuel.2020.117418.
[56] G. Xu, S. Du, J. He, X. Shi, The role of admixed graphene oxide in a cement hydration system, Carbon N. Y. 148 (2019) 141–150, https://doi.org/10.1016/j.carbon.2019.03.072.
[57] A.V. Girão, I.G. Richardson, R. Taylor, R.M.D. Brydson, Composition, morphology and nanostructure of C-S-H in 70% white Portland cement-30% fly ash blends hydrated at 55 °C, Cem. Concr. Res. 40 (2010) 1350–1359, https://doi.org/10.1016/j.cemconres.2010.03.012.
[58] C.A. Love, I.G. Richardson, A.R. Brough, Composition and structure of C-S-H in white Portland cement-20% metakaolin pastes hydrated at 25 °C, Cem. Concr. Res. 37 (2007) 109–117, https://doi.org/10.1016/j.cemconres.2006.11.012.
[59] M.D. Andersen, H.J. Jakobsen, J. Skibsted, A new aluminium-hydrate species in hydrated Portland cements characterized by ^{27}Al and ^{29}Si MAS NMR spectroscopy, Cem. Concr. Res. 36 (2006) 3–17, https://doi.org/10.1016/j.cemconres.2005.04.010.
[60] G. Renaudin, J. Russias, F. Leroux, C. Cau-dit-Coumes, F. Frizon, Structural characterization of C-S-H and C-A-S-H samples-part II: local environment investigated by spectroscopic analyses, J. Solid State Chem. 182 (2009) 3320–3329, https://doi.org/10.1016/j.jssc.2009.09.024.
[61] R.J. Myers, S.A. Bernal, R. San Nicolas, J.L. Provis, Generalized structural description of calcium-sodium aluminosilicate hydrate gels: the cross-linked substituted tobermorite model, Langmuir 29 (2013) 5294–5306, https://doi.org/10.1021/la4000473.
[62] M.Daugaard Andersen, H.J. Jakobsen, Jø. Skibsted, Incorporation of aluminum in the calcium silicate hydrate (C-S-H) of hydrated Portland cements: a high-field ^{27}Al and ^{29}Si MAS NMR investigation, Inorg. Chem. 42 (2003) 2280–2287, https://doi.org/10.1021/ic020607b.
[63] X. Pardal, F. Brunet, T. Charpentier, I. Pochard, A. Nonat, ^{27}Al and ^{29}Si solid-state NMR characterization of calcium-aluminosilicate-hydrate, Inorg. Chem. 51 (3) (2012) 1827–1836, https://doi.org/10.1021/ic202124x.
[64] G.K. Sun, J.F. Young, R.J. Kirkpatrick, The role of Al in C-S–H: NMR, XRD, and compositional results for precipitated samples, Cem. Concr. Res. 36 (2006) 18–29, https://doi.org/10.1016/j.cemconres.2005.03.002.
[65] B. Lothenbach, A. Nonat, Calcium silicate hydrates: solid and liquid phase composition, Cem. Concr. Res. 78 (2015) 57–70, https://doi.org/10.1016/j.cemconres.2015.03.019.
[66] W. Huang, H. Kazemi-Kamyab, W. Sun, K. Scrivener, Effect of cement substitution by limestone on the hydration and microstructural development of ultra-high performance concrete (UHPC), Cem. Concr. Compos. 77 (2017) 86–101, https://doi.org/10.1016/j.cemconcomp.2016.12.009.
[67] Y. Gao, X. Zhu, D.J. Corr, M.S. Konsta-Gdoutos, S.P. Shah, Characterization of the interfacial transition zone of CNF-reinforced cementitious composites, Cem. Concr. Compos. 99 (2019) 130–139, https://doi.org/10.1016/j.cemconcomp.2019.03.002.

[68] R.T. Downs, M. Hall-Wallace, The american mineralogist crystal structure database, Am. Mineral. 88 (2003) 247–250.
[69] R. Alizadeh, L. Raki, J.M. Makar, J.J. Beaudoin, I. Moudrakovski, Hydration of tricalcium silicate in the presence of synthetic calcium–silicate–hydrate, J. Mater. Chem. 19 (2009) 7937–7946, https://doi.org/10.1039/B910216G.
[70] F. Brunet, P. Bertani, T. Charpentier, A. Nonat, J. Virlet, Application of ^{29}Si homonuclear and ^{1}H–^{29}Si heteronuclear NMR correlation to structural studies of calcium silicate hydrates, J. Phys. Chem. B 108 (2004) 15494–15502, https://doi.org/10.1021/jp031174g.
[71] A. Kumar, B.J. Walder, A. Kunhi Mohamed, A. Hofstetter, B. Srinivasan, A. J. Rossini, K. Scrivener, L. Emsley, P. Bowen, The atomic-level structure of cementitious calcium silicate hydrate, J. Phys. Chem. C 121 (2017) 17188–17196, https://doi.org/10.1021/acs.jpcc.7b02439.